## **Ideal Weak Topological Insulator and Protected Helical Saddle Points**

Ji Seop Oh<sup>1,2</sup>, Tianyi Xu<sup>3</sup>, Nikhil Dhale<sup>3</sup>, Sheng Li<sup>3</sup>, Chao Lei<sup>4</sup>, Chiho Yoon<sup>3</sup>, Wenhao Liu<sup>3</sup>, Jianwei Huang<sup>2</sup>, Hanlin Wu<sup>3</sup>, Makoto Hashimoto<sup>5</sup>, Donghui Lu<sup>5</sup>, Chris Jozwiak<sup>6</sup>, Aaron Bostwick<sup>6</sup>, Eli Rotenberg<sup>6</sup>, Chun Ning Lau<sup>7</sup>, Bing Lv<sup>3,\*</sup>, Fan Zhang<sup>3,\*</sup>, Robert Birgeneau<sup>1,8,\*</sup>, Ming Yi<sup>2,\*</sup>

<sup>1</sup>Department of Physics, University of California, Berkeley, California 94720, USA

<sup>2</sup>Department of Physics and Astronomy, Rice University, Houston, Texas 77024, USA

<sup>3</sup>Department of Physics, The University of Texas at Dallas, Richardson, Texas 75080, USA

<sup>4</sup>Department of Physics, The University of Texas at Austin, Austin, Texas 78712, USA

<sup>5</sup>Stanford Synchrotron Radiation Lightsource, SLAC National Accelerator Laboratory, Menlo Park, California 94025, USA

<sup>6</sup>Advanced Light Source, Lawrence Berkeley National Laboratory, Berkeley, California 94720, USA

<sup>7</sup>Department of Physics, The Ohio State University, Columbus, Ohio 43210, USA

<sup>8</sup>Materials Science Division, Lawrence Berkeley National Laboratory, Berkeley, California 94720, USA

## **Abstract**

We report the design and observation of an ideal weak topological insulator in a quasi-one-dimensional bismuth halide,  $Bi_4I_{1.2}Br_{2.8}$ . Via angle-resolved photoemission spectroscopy, we identify that  $Bi_4I_{1.2}Br_{2.8}$  hosts topological surface states on the (100)' side surface in the form of two anisotropic  $\pi$ -offset Dirac cones while topologically dark on the (001) top surface. The results fully determine a unique side-surface Hamiltonian and thereby identify two pairs of non-degenerate helical saddle points. The fact that both the surface Dirac and helical saddle points are in the global bulk band gap of 195 meV suggests potential of this system to be a fertile ground for topological many-body physics.

In three-dimensional (3D) bulk crystals, a strong topological insulator (STI) hosts an odd number of gapless Dirac surface states on every surface, while a weak topological insulator (WTI) has an even number of such surface states on selected surfaces [1–3]. The label "weak" versus "strong" refers to a perception that the topological surface states (TSS) of a WTI could be easily gapped via annihilation of the even number of Dirac cones (DCs) with  $Z_2$  character due to translation symmetry breaking, making a WTI indistinguishable from a trivial insulator whereas a STI is robust [3]. Recent theoretical developments have shown, however, that not only is the gapless nature of WTIs robust to disorder [4–6], but also the initially perceived vulnerability bestows upon WTIs a desired degree of tunability: layer-dimerization gapping TSS in turn gives birth to gapless hinge modes—a mechanism for a topological phase transition into a higher-order topological insulator [7]. Hence, ideal WTIs possess much stronger potential for tunable transitions between 3D topologically distinct phases of matter and, as elucidated below, for realizing two-dimensional topological many-body physics.

Compared to the vast number of identified STIs, WTIs are challenging to realize experimentally, as implied by the two proposed pathways. The first involves periodic stacks of weekly coupled two-dimensional quantum spin Hall insulators where the TSS are located on non-cleavable side surfaces [8]. The second is to engineer a superlattice with multiple band inversions that requires fine tuning of intra- and inter-layer couplings [9,10]. Besides these challenges, TSS in WTIs reported so far, such as ZrTe<sub>5</sub> [11] and RhBi<sub>2</sub> [12], are buried deep in bulk states. Recently, a new series of quasi-one-dimensional (quasi-1D) material bismuth halides Bi<sub>4</sub>X<sub>4</sub> (X = I, Br) with two different naturally cleavable surfaces accessible for ARPES has emerged [7,13–17]. Amongst these,  $\beta$ -Bi<sub>4</sub>I<sub>4</sub> has been identified as a WTI that is only stable above 300 K below which a structural dimerization gaps out the TSS, leading to a higher-order topological insulator [13]. The high temperature range in which the WTI phase is stable makes it challenging to characterize the unique TSS, resulting in controversial angle-resolved photoemission spectroscopy (ARPES) observations and interpretations [13–15].

In order to realize a material platform with stable, tunable, and accessible surface-selective TSS, we designed a WTI in the form of  $Bi_4I_{1.2}Br_{2.8}$  (BIB). Guided by the experimental confirmation that the  $\beta$ -phase is stable in  $Bi_4I_4$  but absent in  $Bi_4Br_4$  [18–20] and by the theoretical prediction that, if

synthesized,  $\beta$ -Bi<sub>4</sub>Br<sub>4</sub> is a WTI superior to  $\beta$ -Bi<sub>4</sub>I<sub>4</sub> because of a larger bulk gap [17], we searched for an optimized substitution ratio between I and Br for a single-stack crystal structure that is stable at all temperatures. We realized this optimization at the ratio of I:Br = 1.2:2.8 and its vicinity (characterization details are in the Supplemental Material [21]). We note that our X-ray refinement and EDX measurements show a single crystalline structure, demonstrating that BIB is a new phase instead of a phase separated mixture of the two end members. The building block of the quasi-1D crystal structure of BIB is the Bi-X chain along the b axis as shown in Fig. 1(a). The chain stacks along both the a and c axes, leading to two distinct natural cleavage planes—the (001) top surface exposing the ab plane and the (20 $\overline{1}$ ) side surface exposing the plane parallel to b and a + 2c. The (20 $\overline{1}$ ) direction in BIB corresponds to (100) in  $\beta$ -Bi<sub>4</sub>I<sub>4</sub>, where the difference originates from the stacking structure. For simplicity we will refer to it as (100)' surface hereafter. Temperature-dependent resistivity curves confirm the lack of a structural distortion down to 2 K in Fig. 1(b). Large single crystals of BIB with extended thickness along both the a and c axes have been grown as shown in Fig. 1(c), allowing direct accesses to the (001) and the (100)' surfaces in ARPES measurements.

Next, we examine the accessibility to the two inequivalent surfaces via ARPES (experimental details are in Supplemental Material [21]). As described above, the absence/presence of TSS for each surface provides definitive evidence for the topological character of a WTI candidate. Figures 2(a) and 2(b) show overviews of momentum-energy dispersions from the (001) and (100)' surfaces, respectively. We observe distinct electronic states, signifying unambiguous single-facet observations for each measurement under a 40 m beam spot. The Fermi surface (FS) map from the (001) surface displays a spot-like feature [Fig. 2(a)], contrary to the parallel line FS across the (100)' surface [Fig. 2(b)]. The clear difference in FS reveals that the interlayer interaction along the a axis is stronger than that along the a axis, consistent with the observations for Bi<sub>4</sub>I<sub>4</sub> [13,15].

Having demonstrated the ability to distinguish the two surfaces, we classify the topological character of each surface (Fig. 2). First from the (001) surface, we investigate band dispersions at the two time-reversal-invariant momenta  $\bar{\Gamma}$  and  $\bar{M}$ . While Fig. 2(c) shows a large gap at  $\bar{\Gamma}$ , at  $\bar{M}$  two spectral features are observed with smaller energy scale in Fig. 2(e)—a valence band top at -0.24 eV

and a conduction band bottom just below the Fermi level,  $E_{\rm F}$ . The conduction band bottom is visible likely due to electron doping from halide vacancies. Both the valence band top and the conduction band bottom are guided by the dotted grey lines in the energy distribution curves (EDCs) in Fig. 2(f). To obtain the band gap at  $\overline{\rm M}$ , we fit the EDC at  $k_{\rm y}=0$ , the red curve in Fig. 2(f), and the gap is determined to be 195 meV with 126 eV photons, varying up to 210 meV with 118 eV photons [21]. Thus, we identify the global bulk gap of 195±10 meV for BIB. Note that the bulk band gap of  $\beta$ -Bi<sub>4</sub>I<sub>4</sub> is smaller than 100 meV [13].

By contrast, the (100)' side surface exhibits surface-originated linear crossings at two different time-reversal-invariant momenta. At both  $\bar{\Gamma}$  and  $\bar{Z}$ , as shown in Figs. 2(g) and 2(j), the band dispersions show linear crossings below  $E_F$  and the crossing at  $\bar{\Gamma}$  appears at -110 meV [Fig. 2(h)] while that at  $\bar{Z}$  appears at -140 meV [Fig. 2(k)]. The energy positions of these crossings do not vary with the photon energy, indicating their surface nature [21]. To demonstrate their gapless nature, we plot the EDCs in Figs. 2(i) and (l) with guides on the band dispersions in grey (cyan) to indicate bulk (surface) state nature. We fit the EDCs at  $k_y = 0$  and  $k_y = \pm 0.01$  Å<sup>-1</sup> [21], and found that two peaks are necessary for EDCs at  $k_y = \pm 0.01$  Å<sup>-1</sup> while only one is needed for  $\bar{\Gamma}$  and  $\bar{Z}$ . Thus, we confirm that the crossings from the (100)' side surface are a pair of gapless TSSs [21].

Taking the observations of the (001) surface and the (100)' surface together, we have demonstrated the necessary conditions to identify BIB as a WTI as illustrated in Figs. 3(a) and 3(b). To verify this, we performed first-principles calculations for BIB. As shown in Fig. 3(c), the bulk electronic states of BIB near  $E_F$  are composed of Bi 6p states. Two band inversions between the interior and exterior Bi  $p_x$  [Fig. 1(a)] bands occur at the L and M points in the 3D Brillouin zone (BZ), which would annihilate when projected onto the (001) surface but be preserved as two linear Dirac crossings when projected onto the (100)' surface. Thus, BIB is a WTI with  $Z_2$  invariants (0;001) based on the Fu-Kane criterion [22].

The existence of two distinct DCs on the (100)' surface, together with the quasi-1D geometry, leads to a unique topological structure with two protected pairs of helical saddle points. To illustrate this, we construct an effective Hamiltonian [7] constrained by the quasi-1D geometry, surface

symmetry, and WTI topology for the (100)' surface states (details in Supplemental Material [21]). The surface states of this minimal model are shown in Fig. 4(a), where there are two pairs of helical saddle points. The presence of these surface saddle points is a direct consequence of the weak dispersion in the stacking direction and the ultimate merger of the two surface DCs. Note that this model is constructed from the experimentally determined crystal structure and informed by the experimentally observed gapless DCs at  $\bar{\Gamma}$  and  $\bar{Z}$ . The presence of the pairs of helical saddle points and the energy gap between  $\bar{\Gamma}$  and  $\bar{Z}$  is guaranteed because the two DCs must be connected between  $\bar{\Gamma}$  and  $\bar{Z}$ , and time-reversal symmetry cannot protect any extra crossing between  $\bar{\Gamma}$  and  $\bar{Z}$ . We note that it is challenging to directly resolve the saddle points separately from the Dirac points, given that the energy and momentum differences between a saddle point and its nearest Dirac point are 4.4 meV and 0.07 Å<sup>-1</sup>, respectively, while the energy resolution of our ARPES experiment is ~20 meV [21].

Having fully constrained the minimal model from a direct comparison of the theoretically calculated and experimentally obtained constant energy surfaces (CESs), shown in Figs. 4(d) and 4(e), respectively, we can now precisely determine the location of the helical saddle points with the Dirac points [Figs. 4(a) and 4(c)]. We also overlay the bulk conduction band (BCB) and bulk valence band (BVB) locations determined previously in Fig. 2(f). As shown in Fig. 4(c), the entire surface state structure is located within the global bulk band gap, which justifies that BIB exhibits the ideal WTI surface characteristics. Interestingly, this TSS gives rise to a series of four potential Lifshitz transitions that can be realized by tuning the chemical potential, as shown by the evolution of the CESs as a function of energy (Fig. 4(d)) [17].

A few remarks are in order. The existence of two pairs of helical saddle points is a part of the topological structure of the unique WTI surface state: the double DCs are  $\pi$ -offset in momentum, which is in sharp contrast to STI with a single surface DC. In BIB, the weak inter-layer coupling ensures the Dirac velocity  $v_z$  to be small and hence the saddle points to be in-gap. Recently, it has been suggested that one can artificially engineer Dirac flat bands by overlaying two STIs with a small twist [23,24], analogous to twisted bilayer graphene [25]. We emphasize that, in an ideal WTI such as BIB, it is naturally guaranteed to host two distinct DCs in the bulk gap with a narrow bandwidth between the two

Van Hove singularities (VHSs). In the case of BIB, this bandwidth is  $\sim 40$  meV, which may be realized by trimerizing the layers or adding spacer layers, both of which are realizable amongst the class of layered bismuth halides. Last but not least, the non-degenerate surface CESs have non-trivial spin texture and can be closed or open.

The exotic topological manifold observed on the side surface of an ideal WTI has potentials to be a fertile ground for topological many-body physics, encouraging further investigations. One example is coupled helical Luttinger-liquid behavior when  $E_F$  is tuned beyond either of the two VHSs but still in the bulk gap where the corresponding CES is open. Indeed, the weak dispersion along the LM direction [Figs. 3(c) and 4] suggests that each (001) monolayer of BIB is a large-gap quantum spin Hall insulator. Appealingly, when such a surface state is proximitized [26] by a linear junction of a ferromagnetic insulator and an s-wave superconductor, a Majorana chain with precisely one Majorana zero mode per layer and uniform nearest-neighbor couplings are expected as shown in Fig. 5(a) [27]. Another example is unconventional indirect exciton condensation when  $E_F$  is tuned to the middle point between the  $\bar{\Gamma}$  and  $\bar{Z}$  Dirac point energies [28]. In this case, the electron and hole pockets are of the same size and thus enjoy perfect nesting as presented in Fig. 4(b). Notably, the spin textures of the two pockets are only half aligned for both the intra- and inter-surface pairing channels, given their helical characteristics as shown in Fig. 5(b) revealed by the effective model.

To summarize, we have designed and discovered an ideal WTI in BIB that is topologically dark on the (001) top surface yet hosts two  $\pi$ -offset DCs and two pairs of helical saddle points on the (100)' side surface. Excitingly, the complete set of topological objects on the (100)' surface state is exposed within the global bulk gap and hence accessible to quantum transport. As the chemical potential of bulk crystals is observed here to be at the edge of the bulk gap, gate tuning allows access to the various regimes in which novel physics is expected, given that gate-tunable boundary transport has recently been achieved in Bi<sub>4</sub>I<sub>4</sub> field effect transistors and Josephson junctions [29]. Superconductivity under hydrostatic pressure have also been reported [30–32]. Altogether, the ideal WTI, BIB, offers a new surface platform for exploring the interplay between band topology and FS instabilities.

## Acknowledgements

This work is mainly supported by National Science Foundation (NSF) through the DMREF program. This research used resources of the Advanced Light Source and the Stanford Synchrotron Radiation Lightsource, both U.S. DOE Office of Science User Facilities under contract Nos. DE-AC02-05CH11231 and DE-AC02-76SF00515, respectively. The work at UC Berkeley is supported by NSF Grant No. DMR-1921798. The work at Rice is supported by NSF under Grant No. DMR-1921847, the Robert A. Welch Foundation under Grant No. C-2024, and the Gordon and Betty Moore Foundation's EPiQS Initiative through grant No. GBMF9470. We acknowledge the Texas Advanced Computing Center (TACC) for providing resources that have contributed to the research results reported in this work. The work at UT Dallas is supported by NSF under Grant Nos. DMR-1921581 and DMR-1945351, AFOSR under Grant No. FA9550-19-1-0037, and Army Research Office (ARO) under Grant No. W911NF-18-1-0416.

## References

- [1] J. E. Moore and L. Balents, Topological Invariants of Time-Reversal-Invariant Band Structures, Phys. Rev. B **75**, 121306 (2007).
- [2] R. Roy, Topological Phases and the Quantum Spin Hall Effect in Three Dimensions, Phys. Rev. B **79**, 195322 (2009).
- [3] L. Fu, C. L. Kane, and E. J. Mele, Topological Insulators in Three Dimensions, Phys. Rev. Lett. **98**, 106803 (2007).
- [4] Z. Ringel, Y. E. Kraus, and A. Stern, Strong Side of Weak Topological Insulators, Phys. Rev. B **86**, 045102 (2012).
- [5] R. S. K. Mong, J. H. Bardarson, and J. E. Moore, Quantum Transport and Two-Parameter Scaling at the Surface of a Weak Topological Insulator, Phys. Rev. Lett. **108**, 076804 (2012).
- [6] L. Fu and C. L. Kane, Topology, Delocalization via Average Symmetry and the Symplectic Anderson Transition, Phys. Rev. Lett. **109**, 246605 (2012).
- [7] C. Yoon, C.-C. Liu, H. Min, and F. Zhang, Quasi-One-Dimensional Higher-Order Topological Insulators, ArXiv200514710 Cond-Mat (2020).
- [8] B. Rasche, A. Isaeva, M. Ruck, S. Borisenko, V. Zabolotnyy, B. Büchner, K. Koepernik, C. Ortix, M. Richter, and J. van den Brink, Stacked Topological Insulator Built from Bismuth-Based Graphene Sheet Analogues, Nat. Mater. 12, 422 (2013).
- [9] X. Li, F. Zhang, Q. Niu, and J. Feng, Superlattice Valley Engineering for Designer Topological Insulators, Sci. Rep. 4, 6397 (2014).
- [10] G. Yang, J. Liu, L. Fu, W. Duan, and C. Liu, Weak Topological Insulators in PbTe/SnTe Superlattices, Phys. Rev. B **89**, 085312 (2014).
- [11] P. Zhang *et al.*, Observation and Control of the Weak Topological Insulator State in ZrTe<sub>5</sub>, Nat. Commun. **12**, 406 (2021).
- [12] K. Lee *et al.*, Discovery of a Weak Topological Insulating State and van Hove Singularity in Triclinic RhBi<sub>2</sub>, Nat. Commun. **12**, 1855 (2021).
- [13] J. Huang *et al.*, Room-Temperature Topological Phase Transition in Quasi-One-Dimensional Material Bi<sub>4</sub>I<sub>4</sub>, Phys. Rev. X **11**, 031042 (2021).
- [14] G. Autès *et al.*, A Novel Quasi-One-Dimensional Topological Insulator in Bismuth Iodide  $\beta$ -Bi<sub>4</sub>I<sub>4</sub>, Nat. Mater. **15**, 154 (2016).
- [15] R. Noguchi *et al.*, A Weak Topological Insulator State in Quasi-One-Dimensional Bismuth Iodide, Nature **566**, 518 (2019).
- [16] R. Noguchi *et al.*, Evidence for a Higher-Order Topological Insulator in a Three-Dimensional Material Built from van Der Waals Stacking of Bismuth-Halide Chains, Nat. Mater. **20**, 473 (2021)
- [17] C.-C. Liu, J.-J. Zhou, Y. Yao, and F. Zhang, Weak Topological Insulators and Composite Weyl Semimetals:  $\beta$ -Bi<sub>4</sub>X<sub>4</sub> (X = Br, I), Phys. Rev. Lett. **116**, 066801 (2016).
- [18] H. G. von Schnering, H. von Benda, and C. Kalveram, Wismutmonojodid BiJ, eine Verbindung mit Bi(O) und Bi(II), Z. Für Anorg. Allg. Chem. **438**, 37 (1978).
- [19] H. von Benda, A. Simon, and W. Bauhofer, Zur Kenntnis von BiBr und BiBr<sub>1,167</sub>, Z. Für Anorg. Allg. Chem. **438**, 53 (1978).
- [20] T. G. Filatova, P. V. Gurin, L. Kloo, V. A. Kulbachinskii, A. N. Kuznetsov, V. G. Kytin, M. Lindsjo, and B. A. Popovkin, Electronic Structure, Galvanomagnetic and Magnetic Properties of the Bismuth Subhalides Bi<sub>4</sub>I<sub>4</sub> and Bi<sub>4</sub>Br<sub>4</sub>, J. Solid State Chem. **180**, 1103 (2007).
- [21] See the Supplementary Materials. which also includes Refs. [33–37].
- [22] L. Fu and C. L. Kane, Topological Insulators with Inversion Symmetry, Phys. Rev. B **76**, 045302 (2007).
- [23] J. Cano, S. Fang, J. H. Pixley, and J. H. Wilson, Moiré Superlattice on the Surface of a Topological Insulator, Phys. Rev. B **103**, 155157 (2021).
- [24] T. Wang, N. F. Q. Yuan, and L. Fu, Moiré Surface States and Enhanced Superconductivity in Topological Insulators, Phys. Rev. X 11, 021024 (2021).
- [25] C. N. Lau, M. W. Bockrath, K. F. Mak, and F. Zhang, Reproducibility in the Fabrication and Physics of Moiré Materials, Nature **602**, 41 (2022).

- [26] L. Fu and C. L. Kane, Superconducting Proximity Effect and Majorana Fermions at the Surface of a Topological Insulator, Phys. Rev. Lett. **100**, 096407 (2008).
- [27] Y.-F. Zhou and F. Zhang, private communications on their manuscript in preparation.
- [28] P. Rickhaus *et al.*, Correlated Electron-Hole State in Twisted Double-Bilayer Graphene, Science **373**, 1257 (2021).
- [29] Y. Liu *et al.*, Gate-Tunable Transport in Quasi-One-Dimensional α-Bi<sub>4</sub>I<sub>4</sub> Field Effect Transistors, Nano Lett. **22**, 1151 (2022).
- [30] A. Pisoni, R. Gaál, A. Zeugner, V. Falkowski, A. Isaeva, H. Huppertz, G. Autès, O. V. Yazyev, and L. Forró, Pressure Effect and Superconductivity in the β-Bi<sub>4</sub>I<sub>4</sub> Topological Insulator, Phys. Rev. B **95**, 235149 (2017).
- [31] Y. Qi *et al.*, Pressure-Induced Superconductivity and Topological Quantum Phase Transitions in a Quasi-One-Dimensional Topological Insulator: Bi<sub>4</sub>I<sub>4</sub>, Npj Quantum Mater. **3**, 4 (2018).
- [32] X. Li *et al.*, Pressure-Induced Phase Transitions and Superconductivity in a Quasi–1-Dimensional Topological Crystalline Insulator α-Bi 4 Br 4, Proc. Natl. Acad. Sci. **116**, 17696 (2019).
- [33] G. Kresse and J. Furthmüller, Efficient Iterative Schemes for *Ab Initio* Total-Energy Calculations Using a Plane-Wave Basis Set, Phys. Rev. B **54**, 11169 (1996).
- [34] J. P. Perdew, K. Burke, and M. Ernzerhof, Generalized Gradient Approximation Made Simple, Phys. Rev. Lett. 77, 3865 (1996).
- [35] G. Kresse and D. Joubert, From Ultrasoft Pseudopotentials to the Projector Augmented-Wave Method, Phys. Rev. B **59**, 1758 (1999).
- [36] J. Heyd, G. E. Scuseria, and M. Ernzerhof, Hybrid Functionals Based on a Screened Coulomb Potential, J. Chem. Phys. 118, 8207 (2003).
- [37] L. Nordheim, Zur Elektronentheorie der Metalle. II, Ann. Phys. 401, 641 (1931).

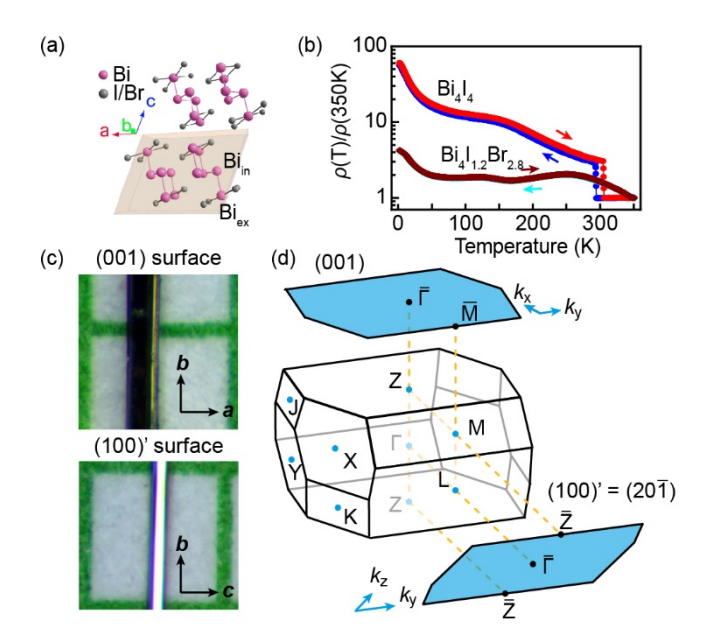


FIG. 1 (a) Crystal structure of BIB. A parallelepiped shows the unit cell. (b) Temperature-dependent resistivity for  $Bi_4I_4$  and BIB. (c) Images for BIB crystals showing the accessible top (001) and side (100)' surfaces. The size of the grid is  $1 \times 1 \text{ mm}^2$ . (d) Bulk BZ and the (001) and (100)' surface BZs.

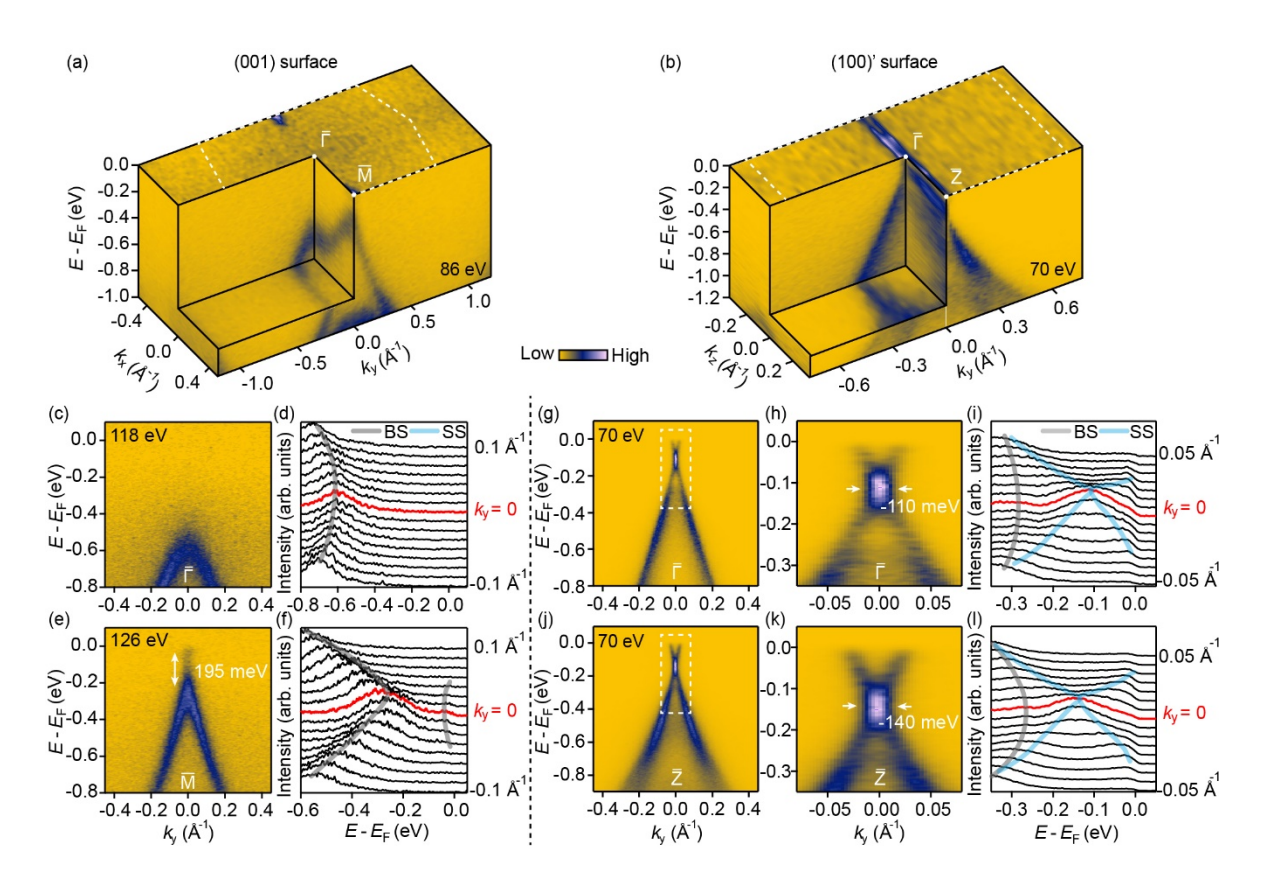


FIG. 2 (a) Overview of ARPES spectra with band dispersions across high symmetry points and FS maps on the (001) and (100)' surfaces. 86 eV and 70 eV photons were used for the (001) and (100)' surfaces, respectively. (c) and (d) Band dispersion across  $\bar{\Gamma}$  on the (001)-projected surface BZ and the corresponding EDCs. (e) and (f) Analogous plots to (c) and (d) at  $\bar{M}$  on the (001) surface. (g) Band dispersions across  $\bar{\Gamma}$  on the (100)'-projected surface BZ. (h) Zoomed-in view of the white box in (g), showing the Dirac crossing at -110 meV. (i) corresponding EDCs from (h). (j)–(l) Equivalent plots as (g)–(i) for the  $\bar{Z}$  point on the (100)'-projected surface BZ with a Dirac crossing at -140 meV.

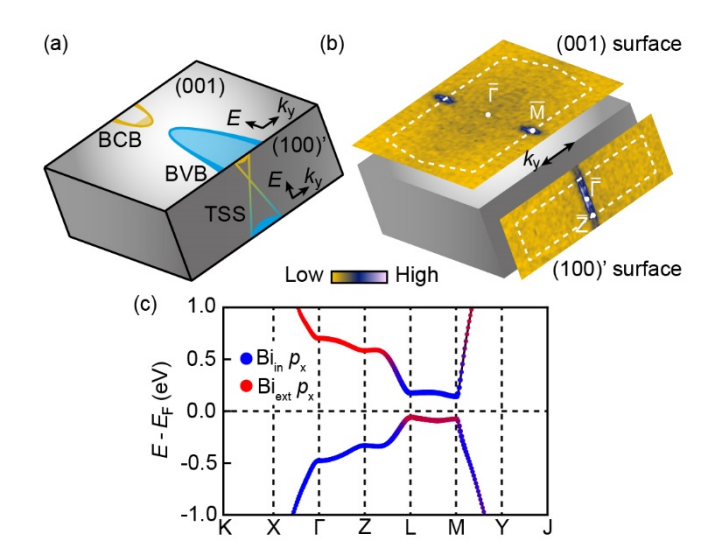


FIG. 3 (a) A schematic overview for the WTI nature of BIB based on experimental observations. (b) FSs measured on the (001) and (100)' surfaces. (c) First-principles bulk calculations for BIB.

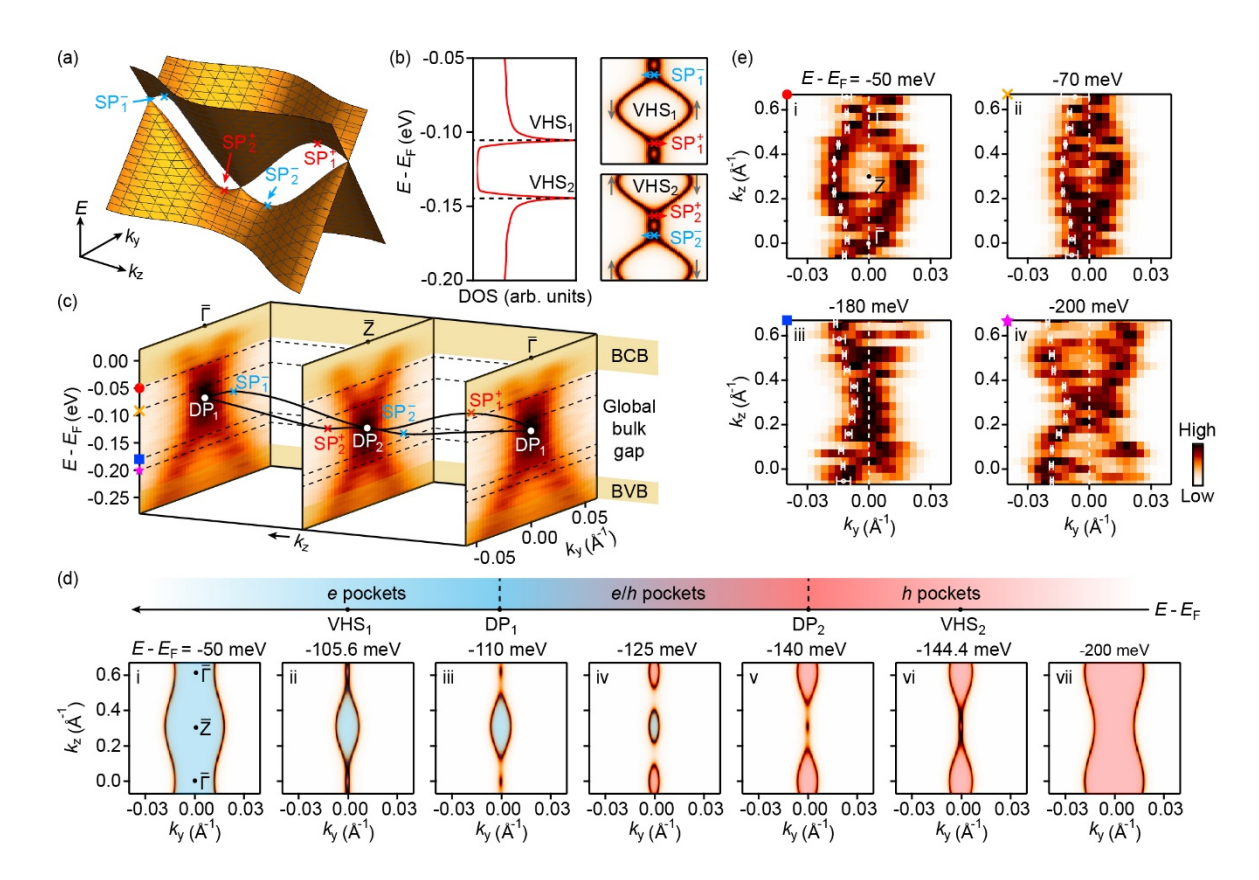


FIG. 4 (a) 3D electronic structure given by the minimal model. Two pairs of helical saddle points are labeled as  $SP_{1,2}^{\pm}$ . Subscripts 1 (2) indicate the energy location higher (lower) than that of the Dirac points, and superscripts  $\pm$  indicate the spin polarizations. (b) Left: Calculated surface state density of states using the minimal model. Two saddle-point Van Hove singularities (VHS<sub>1,2</sub>) are shown. Right: Spin textures on CESs at VHS<sub>1,2</sub>. (c) 3D plot for a comprehensive description of the electronic structure on the (100)' surface.  $DP_{1,2}$  show the Dirac points at  $\bar{\Gamma}$  and  $\bar{Z}$ , respectively. (d) CESs obtained from the minimal model at key energies indicated by the bar along the energy axis. Shades on CESs indicate electron- (blue) and hole- (red) pockets. (e) Experimentally obtained CESs above and below VHS<sub>1,2</sub> and  $DP_{1,2}$ . Colored marks on the left top corners indicate the energy positions in (c). White dots with error bars (standard deviation for the results) are fitted positions of CESs.

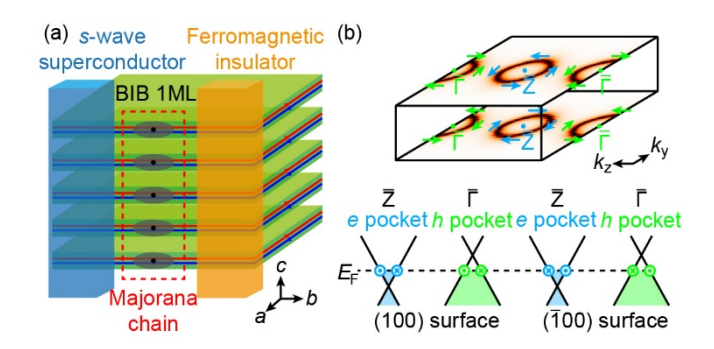


FIG. 5 (a) Emergence of Majorana chain when the (100)' TSS is proximitized to a linear junction of a ferromagnetic insulator and an *s*-wave superconductor. (b) Unconventional exciton condensation by perfect nesting condition between electron and hole pockets in the TSS where their spin textures are only half-aligned for both the intra- and inter-surface pairing channels.